

Simulations of Optical Microscope Images

Thomas A. Germer^a and Egon Marx^b

^a*Optical Technology Division, National Institute of Standards and Technology, Gaithersburg, MD 20899*

^b*Precision Engineering Division, National Institute of Standards and Technology, Gaithersburg, MD 20899*

ABSTRACT

The resolution of an optical microscope is limited by the optical wavelengths used. However, there is no fundamental limit to the sensitivity of a microscope to small differences in any of a feature's dimensions. That is, those limits are determined by such things as the sensitivity of the detector array, the quality of the optical system, and the stability of the light source. The potential for using this nearly unbounded sensitivity has sparked interest in extending optical microscopy to the characterization of sub-wavelength structures created by photolithography and using that characterization for process control. In this paper, an analysis of the imaging of a semiconductor grating structure with an optical microscope will be presented. The analysis includes the effects of partial coherence in the illumination system, aberrations of both the illumination and the collection optics, non-uniformities in the illumination, and polarization. It can thus model just about any illumination configuration imaginable, including Köhler illumination, focused (confocal) illumination, or dark-field illumination. By propagating Jones matrices throughout the system, polarization control at the back focal planes of both illumination and collection can be investigated. Given a detailed characterization of the microscope (including aberrations), images can be calculated and compared to real data, allowing details of the grating structure to be determined, in a manner similar to that found in scatterometry.

Keywords: coherence, imaging, lithography, microscopy, polarization, scatter

1. INTRODUCTION

For many years, optical microscopy has been used for determining dimensions of structures and assessing the overlay between structures in different layers. As structures become smaller, such that they become of the order of or smaller than the optical wavelength, optical microscopy's ability to perform this metrology comes into question. However, other optical methods, such as grating scatterometry, diffuse light scattering, and interferometry, have all demonstrated sub-wavelength sensitivity. They each owe their sensitivity to the ability for electromagnetic theory to predict their behavior, that theory being nearly trivial in interferometry, but more complicated in grating scatterometry or diffuse light scattering. With today's computational tools, however, optical microscopy can potentially join this class of sensitive techniques, provided that all aspects of the measurement that determine the response are understood and can be predicted.¹

In this manuscript, we outline the theory required to calculate optical images of structures on surfaces and apply it to line gratings. Since the simulations of gratings with the electromagnetic fields is performed using a plane-wave basis, we make a point of treating the entire microscope, from source to image, using plane waves. We also maintain information about polarization throughout the simulation, consider coherence effects in the source, and include aberrations. We thus avoid some of the errors that might be made by assuming a simple scalar point-spread function for the optical response. While the method described is a forward calculation of the image, a library of images as a function of the sample and measurement parameters can be developed and used in a manner similar to that often used in grating scatterometry.

2. THEORY

In this section, we describe the method we use to calculate an image in a microscope. In Subsec. 2.1, we briefly describe two methods that we use to calculate the scattering properties of a structure. These methods, being solutions to Maxwell's equations, are inherently wave-like in their descriptions, and it would be inappropriate to use a ray optic approach to propagating light in the microscope. Thus, we are left attempting to describe propagation from the light source through the illumination system, scattering from the sample, and propagation to the imaging detector using an entirely plane-wave approach. In Subsec. 2.2, we describe sets of unit vectors that we will use as bases to describe the field vec-

tors. In Subsec. 2.3, we describe the propagation of a field from an object plane to an image plane in an aberration-free optical system. In Subsec. 2.4, we describe the calculation of the image intensity. We then describe the illumination field in Subsec. 2.5, where we account for the finitely illuminated region on the sample. Since the approach for calculating the image intensity in Subsec. 2.4 does not describe the effects that polarization might have on the image, we describe in Subsec. 2.6 an approach for calculating a Mueller matrix image, from which the image from any combination of incident and collection polarizations can be calculated. Finally, in Subsec. 2.7, we discuss how we account for aberrations.

2.1. Sample scattering

There are a number of methods used to calculate the relationship between the incident and scattered plane waves. The two methods which are used here are an implementation of rigorous coupled wave analysis (RCWA) and an integral equation solution (IES). The RCWA method solves Maxwell's equations with periodic boundary conditions, and thus can only be applied to periodic structures.^{2,3} The IES method solves Maxwell's equations on a finite structure on an infinite substrate, making the method most useful for isolated features.¹ However, both methods can be applied to similar structures, provided that a large enough period is used in RCWA or that enough repeated structures are used in IES. The solution in RCWA is expressed as amplitudes for a discrete set of plane waves, while that for IES is expressed as the field evaluated along some line evaluated from the sum of a reflected plane wave and the integral of cylindrical waves. Details of the two methods are given elsewhere.¹⁻³

2.2. Polarization basis sets

Since electromagnetic waves are transverse in nature, and since we will express all waves in terms of a plane-wave decomposition, it is useful to assign a set of transverse basis vectors for which we define a polarization for any wavevector \mathbf{k} . We can define two unit vectors $\hat{\mathbf{e}}_s(\mathbf{k})$ and $\hat{\mathbf{h}}_p(\mathbf{k})$, which are perpendicular to \mathbf{k} and have no z-component,

$$\hat{\mathbf{e}}_s(\mathbf{k}) = -\hat{\mathbf{h}}_p(\mathbf{k}) = \left(-k_y / \sqrt{k_x^2 + k_y^2}, k_x / \sqrt{k_x^2 + k_y^2}, 0 \right). \quad (1)$$

We define two more vectors, $\hat{\mathbf{e}}_p(\mathbf{k})$ and $\hat{\mathbf{h}}_s(\mathbf{k})$, which are perpendicular to $\hat{\mathbf{e}}_s(\mathbf{k})$ and $\hat{\mathbf{h}}_p(\mathbf{k})$ and to \mathbf{k} ,

$$\hat{\mathbf{e}}_p(\mathbf{k}) = \hat{\mathbf{h}}_s(\mathbf{k}) = \left(-k_x k_z / \sqrt{k_x^2 + k_y^2}, -k_y k_z / \sqrt{k_x^2 + k_y^2}, \sqrt{k_x^2 + k_y^2} \right) / k. \quad (2)$$

The four vectors in Eqs. (1) and (2) follow

$$\hat{\mathbf{e}}_s \times \hat{\mathbf{e}}_p = \mathbf{k} / k, \quad \hat{\mathbf{h}}_s \times \hat{\mathbf{h}}_p = \mathbf{k} / k, \quad \hat{\mathbf{e}}_s \times \hat{\mathbf{h}}_s = \mathbf{k} / k, \quad \hat{\mathbf{e}}_p \times \hat{\mathbf{h}}_p = \mathbf{k} / k, \quad \hat{\mathbf{e}}_s \cdot \hat{\mathbf{e}}_p = 0, \quad \hat{\mathbf{h}}_s \cdot \hat{\mathbf{h}}_p = 0. \quad (3)$$

We can define the z-axis in any way that we would like. However, for this paper, it is convenient to define the z-axis to be along the rotational axis of the optical system. The vectors $\hat{\mathbf{e}}_s$ and $\hat{\mathbf{h}}_s$ can then be used to define the electric and magnetic fields, respectively, for what we call s-polarized light, while $\hat{\mathbf{e}}_p$ and $\hat{\mathbf{h}}_p$ can be used to define the electric and magnetic fields, respectively, for what we call p-polarized light.

Another useful set of vectors, which are suitable for defining polarization at the source or at the detector, where light is propagating primarily in the z-direction, is

$$\hat{\mathbf{e}}_x = -\hat{\mathbf{h}}_y = (1, 0, 0), \quad \hat{\mathbf{e}}_y = \hat{\mathbf{h}}_x = (0, 1, 0). \quad (4)$$

2.3. Propagation of light through the microscope

In a semi-infinite free-space, with no sources at infinity, we can decompose any monochromatic electric field into a spectrum, $\mathbf{A}(\boldsymbol{\kappa})$, such that

$$\mathbf{E}(\boldsymbol{\rho}, z) = \int d^2\boldsymbol{\kappa} \mathbf{A}(\boldsymbol{\kappa}) e^{i(\boldsymbol{\kappa} \cdot \boldsymbol{\rho} + k_z z)}, \quad (5)$$

where the location is given by $\mathbf{r} = (\boldsymbol{\rho}, z)$, $\boldsymbol{\rho} = (x, y)$, the wavevector is $\mathbf{k} = (\boldsymbol{\kappa}, k_z)$, $\boldsymbol{\kappa} = (k_x, k_y)$, and

$$\mathbf{A}(\boldsymbol{\kappa}) = \frac{1}{4\pi^2} \int d^2\boldsymbol{\rho} \mathbf{E}(\boldsymbol{\rho}, 0) e^{-i\boldsymbol{\kappa}\cdot\boldsymbol{\rho}}. \quad (6)$$

The $\exp(-i\omega t)$ dependence upon time is implied, where $\omega = k/\sqrt{\varepsilon_0\mu_0}$. Since electromagnetic waves are transverse, we can further decompose the spectrum into two orthogonal polarization components,

$$\mathbf{A}(\boldsymbol{\kappa}) = A_s(\boldsymbol{\kappa})\hat{\mathbf{e}}_s(\mathbf{k}) + A_p(\boldsymbol{\kappa})\hat{\mathbf{e}}_p(\mathbf{k}), \quad (7)$$

where

$$A_j(\boldsymbol{\kappa}) = \mathbf{A}(\boldsymbol{\kappa}) \cdot \hat{\mathbf{e}}_j(\mathbf{k}). \quad (8)$$

The optics in a microscope redirect waves from the object plane onto the image plane and appropriately set the phase and amplitude of those waves. That is, the optical system provides a mapping of wavevector, $\mathbf{g}: \{\mathbf{k}\} \rightarrow \{\mathbf{k}'\}$, and a mapping of the field spectrum, $\mathbf{f}: \{\mathbf{A}(\boldsymbol{\kappa})\} \rightarrow \{\mathbf{A}'(\boldsymbol{\kappa}')\}$. The electric field near the image plane is then given by

$$\mathbf{E}'(\boldsymbol{\rho}', z') = \int d^2\boldsymbol{\kappa}' \mathbf{A}'(\boldsymbol{\kappa}') e^{i(\boldsymbol{\kappa}'\cdot\boldsymbol{\rho}'+k'_z z')}, \quad (9)$$

where $\boldsymbol{\rho}' = (x', y')$ and z' are coordinates near the image plane. In an aberration-free optical system, the function \mathbf{g} between \mathbf{k} and $\mathbf{k}' = (\boldsymbol{\kappa}', k'_z) = \mathbf{g}(\mathbf{k})$ is

$$\mathbf{g}(\mathbf{k}) = \left(-\boldsymbol{\kappa}/M, \sqrt{k^2 - |\boldsymbol{\kappa}/M|^2} \right) \quad (10)$$

where M is the magnification of the system. Due to the rotational symmetry about the optical axis, s-polarized light remains s-polarized and p-polarized light remains p-polarized. Furthermore, energy contained in a plane wave leaving a given area at the object plane will impinge upon an area M^2 larger at the image plane, and the beam will have a cross sectional area $M^2 k'_z/k_z$ larger. Thus, the function $\mathbf{A}'(\mathbf{k}') = \mathbf{f}(\mathbf{A}, \boldsymbol{\kappa})$ can be expressed in terms of a dyadic

$$\mathbf{f}(\mathbf{A}, \boldsymbol{\kappa}) = \frac{1}{M} \left(\frac{k_z}{k'_z} \right)^{1/2} \times \begin{cases} [\hat{\mathbf{e}}_s(\mathbf{k}')\hat{\mathbf{e}}_s(\mathbf{k}) + \hat{\mathbf{e}}_p(\mathbf{k}')\hat{\mathbf{e}}_p(\mathbf{k})] \cdot \mathbf{A}(\boldsymbol{\kappa}) & : |\boldsymbol{\kappa}|/k < \text{NA} \\ 0 & : |\boldsymbol{\kappa}|/k \geq \text{NA} \end{cases} \quad (11)$$

The matrix form of Eq. (11) for $|\boldsymbol{\kappa}|/k < \text{NA}$ is

$$\mathbf{f}(\mathbf{A}, \boldsymbol{\kappa}) = \frac{1}{k^2(k_x^2 + k_y^2)} \left(\frac{k_z}{k'_z} \right)^{1/2} \begin{pmatrix} k^2 k_y k'_y + k_x k'_x k_z k'_z & -k^2 k_x k'_y + k_y k'_x k_z k'_z & -k'_x k'_z (k_x^2 + k_y^2) \\ -k^2 k_y k'_x + k_x k'_y k_z k'_z & k^2 k_x k'_x + k_y k'_y k_z k'_z & -k'_y k'_z (k_x^2 + k_y^2) \\ -k_x k_z (k_x'^2 + k_y'^2) & -k_y k_z (k_x'^2 + k_y'^2) & (k_x^2 + k_y^2)(k_x'^2 + k_y'^2) \end{pmatrix} \begin{pmatrix} A_x \\ A_y \\ A_z \end{pmatrix}. \quad (12)$$

An equivalent discussion can be carried out with magnetic fields. The transformation between the magnetic field spectral components is the same as Eq. (12). In the limit of large magnification, Eq. (12) reduces in lowest order of $1/M$ to

$$\mathbf{f}(\mathbf{A}, \boldsymbol{\kappa}) \cong \frac{1}{Mk(k_x^2 + k_y^2)} \left(\frac{k_z}{k} \right)^{1/2} \begin{pmatrix} -kk_y^2 - k_x^2 k_z & k_x k_y (k - k_z) & k_x (k_x^2 + k_y^2) \\ k_y k_x (k - k_z) & -kk_x^2 - k_y^2 k_z & k_y (k_x^2 + k_y^2) \\ 0 & 0 & 0 \end{pmatrix} \begin{pmatrix} A_x \\ A_y \\ A_z \end{pmatrix} \quad (13)$$

For unit magnification and using the fact that $\mathbf{A}(\boldsymbol{\kappa}) \cdot \mathbf{k} = 0$, Eq. (12) reduces to

$$\mathbf{f}(\mathbf{A}, \boldsymbol{\kappa}) = \begin{pmatrix} -1 & 0 & 0 \\ 0 & -1 & 0 \\ 0 & 0 & 1 \end{pmatrix} \begin{pmatrix} A_x \\ A_y \\ A_z \end{pmatrix} \quad (14)$$

2.4. Intensity

We now define $\mathbf{E}_j(\boldsymbol{\rho}, z, \boldsymbol{\kappa}^{\text{inc}})$ to be the field amplitude at $\boldsymbol{\rho}$ and z given a unit amplitude j -polarized field incident on the sample with wavevector $\boldsymbol{\kappa}^{\text{inc}}$. The total field near the image plane is then

$$\mathbf{E}^{\text{tot}}(\boldsymbol{\rho}', z') = \sum_{j=s,p} \int d^2\boldsymbol{\kappa}^{\text{inc}} \mathbf{E}_j(\boldsymbol{\rho}', z', \boldsymbol{\kappa}^{\text{inc}}) A_j^{\text{inc}}(\boldsymbol{\kappa}^{\text{inc}}), \quad (15)$$

where $A_j^{\text{inc}}(\boldsymbol{\kappa}^{\text{inc}})$ is the spectrum of the field incident upon the sample. The total intensity near the detector plane is

$$I(\boldsymbol{\rho}', z') = \varepsilon_0 \langle [\mathbf{E}^{\text{tot}}(\boldsymbol{\rho}', z')]^* \cdot \mathbf{E}^{\text{tot}}(\boldsymbol{\rho}', z') \rangle. \quad (16)$$

The brackets in Eq. (16) signify that an average is to be taken over fluctuations in the incident light spectrum. If the sample is stationary, we can combine Eqs. (15) and (16) to get the intensity

$$I(\boldsymbol{\rho}', z') = \varepsilon_0 \sum_{j,k=s,p} \int d^2\boldsymbol{\kappa}_1 d^2\boldsymbol{\kappa}_2 \mathbf{E}_j^*(\boldsymbol{\rho}', z', \boldsymbol{\kappa}_1) \cdot \mathbf{E}_k(\boldsymbol{\rho}', z', \boldsymbol{\kappa}_2) \langle A_j^{\text{inc}*}(\boldsymbol{\kappa}_1) A_k^{\text{inc}}(\boldsymbol{\kappa}_2) \rangle. \quad (17)$$

We thus need the coherence function, $\langle A_j^{\text{inc}*}(\boldsymbol{\kappa}_1) A_k^{\text{inc}}(\boldsymbol{\kappa}_2) \rangle$, for the illumination.

2.5. Illumination

Consider a circular aperture of diameter D , inside of which the field is random with a correlation length ξ , and outside of which the field is zero:

$$\langle \mathbf{E}^{\text{src}*}(\boldsymbol{\rho}) \cdot \mathbf{E}^{\text{src}}(\boldsymbol{\rho}') \rangle = \begin{cases} |\mathbf{E}_0^{\text{src}}|^2 \exp(-|\boldsymbol{\rho} - \boldsymbol{\rho}'|^2 / \xi^2) & : |\boldsymbol{\rho}| < D/2 \text{ and } |\boldsymbol{\rho}'| < D/2 \\ 0 & : |\boldsymbol{\rho}| \geq D/2 \text{ or } |\boldsymbol{\rho}'| \geq D/2 \end{cases}. \quad (18)$$

From Eq. (6) and letting ξ be very small, the angular correlation function is

$$\langle A_j^{\text{src}*}(\boldsymbol{\kappa}) A_k^{\text{src}}(\boldsymbol{\kappa}') \rangle \cong \frac{D\xi^2 |\mathbf{E}_0^{\text{src}}|^2}{4} \frac{J_1(D|\boldsymbol{\kappa} - \boldsymbol{\kappa}'|/2)}{|\boldsymbol{\kappa} - \boldsymbol{\kappa}'|} \delta_{jk} \quad (19)$$

($j, k = s, p$), where $J_1(x)$ is the first-order Bessel function of the first kind, and δ_{jk} is the Kronecker delta. The angular intensity in the j -th polarization,

$$\langle |A_j^{\text{src}}(\boldsymbol{\kappa})|^2 \rangle = \lim_{\boldsymbol{\kappa}' \rightarrow \boldsymbol{\kappa}} \langle A_j^{\text{src}*}(\boldsymbol{\kappa}) A_j^{\text{src}}(\boldsymbol{\kappa}') \rangle = \frac{D^2 \xi^2 |\mathbf{E}_0^{\text{src}}|^2}{16}, \quad (20)$$

is uniform. In the case of *critical illumination*, the illumination optics image the source onto the sample. Using the image calculations described in Subsec. 2.3 above, for small magnification, we find after some algebra that the coherence function at the sample is

$$\langle A_j^{\text{illum}*}(\boldsymbol{\kappa}) A_k^{\text{illum}}(\boldsymbol{\kappa}') \rangle = \frac{DM^{\text{illum}} \xi^2 |\mathbf{E}_0^{\text{src}}|^2}{4\sqrt{k_z k'_z}} \frac{k J_1(D|\boldsymbol{\kappa} - \boldsymbol{\kappa}'| M^{\text{illum}}/2)}{|\boldsymbol{\kappa} - \boldsymbol{\kappa}'|} \delta_{jk}. \quad (21)$$

When $DM^{\text{illum}} k \gg 1$, Eq. (21) may be approximated in an integral by

$$\langle A_j^{\text{illum}*}(\boldsymbol{\kappa}) A_k^{\text{illum}}(\boldsymbol{\kappa}') \rangle = \frac{\pi \xi^2 k |\mathbf{E}_0^{\text{src}}|^2}{k_z} \delta(\boldsymbol{\kappa} - \boldsymbol{\kappa}') \delta_{jk}. \quad (22)$$

Note the factor of k_z in the denominator. In the case of *Köhler illumination*, the illumination optics image the source onto the back focal plane, instead of the sample, and the back focal plane is uniformly illuminated. A field stop still exists in the system to define the illumination diameter at the sample. Eq. (20) suggests that in critical illumination the back focal plane is also uniformly illuminated. Furthermore, an analysis by Born and Wolf demonstrates that the coherence associated with the critical and Köhler illumination schemes are identical. We will therefore assume that the two cases are the same and use Eqs. (21) or (22) to calculate images.

For the correlation function given in Eq. (22), the intensity at the detector is

$$I(\boldsymbol{\rho}', z') = \frac{\pi \xi^2 k \varepsilon |\mathbf{E}_0^{\text{src}}|^2}{(M^{\text{illum}})^2} \sum_{j=s,p} \int d^2 \boldsymbol{\kappa} \frac{|\mathbf{E}_j^*(\boldsymbol{\rho}', z', \boldsymbol{\kappa})|^2}{k_z}. \quad (23)$$

2.6. Polarimetry

We present another approach to the calculation of the intensity, which allows for a treatment of polarization and coherence in a unified manner. Let us assume that we have scattering matrices $\mathbf{S}(\boldsymbol{\rho}, \mathbf{k}_i)$ that relate the amplitudes of the field incident upon the sample to the amplitudes of the field at the image plane. The vector $\boldsymbol{\rho}$ is the position on the detector array, and \mathbf{k}_i is the incident wavevector. We define four matrices described by the following dyadics,

$$\boldsymbol{\sigma}_0 = \mathbf{e}_x \mathbf{e}_x + \mathbf{e}_y \mathbf{e}_y, \quad \boldsymbol{\sigma}_1 = \mathbf{e}_x \mathbf{e}_x - \mathbf{e}_y \mathbf{e}_y, \quad \boldsymbol{\sigma}_2 = \mathbf{e}_y \mathbf{e}_x + \mathbf{e}_x \mathbf{e}_y, \quad \boldsymbol{\sigma}_3 = i[\mathbf{e}_y \mathbf{e}_x - \mathbf{e}_x \mathbf{e}_y], \quad (24)$$

and an operation, which returns a four element vector whose j -th component is

$$[\boldsymbol{\Sigma}(\mathbf{A}_1^\dagger, \mathbf{A}_2)]_j = \mathbf{A}_1^\dagger \cdot \boldsymbol{\sigma}_j \cdot \mathbf{A}_2 \quad (25)$$

($j = 0, 1, 2, 3$). The four-element vector $\boldsymbol{\Sigma}(\mathbf{A}^\dagger, \mathbf{A})$ is the Stokes vector representation of the field amplitude \mathbf{A} .⁴ The total field is given by

$$\mathbf{E}^{\text{tot}}(\boldsymbol{\rho}, z) = \int d^2 \boldsymbol{\kappa}^{\text{inc}} \mathbf{S}(\boldsymbol{\rho}, \boldsymbol{\kappa}^{\text{inc}}) \cdot \mathbf{A}^{\text{inc}}(\boldsymbol{\kappa}^{\text{inc}}). \quad (26)$$

The average net Stokes vector intensity is given by substituting Eq. (26) into Eq. (25) and averaging,

$$\begin{aligned} \mathbf{I}^{\text{tot}}(\boldsymbol{\rho}, z) &= \varepsilon \left\langle \boldsymbol{\Sigma} \left[\int d^2 \boldsymbol{\kappa}^{\text{rinc}} \mathbf{A}^{\text{rinc}}(\boldsymbol{\kappa}^{\text{rinc}}) \cdot \mathbf{S}^\dagger(\boldsymbol{\rho}, \boldsymbol{\kappa}^{\text{rinc}}), \int d^2 \boldsymbol{\kappa}^{\text{inc}} \mathbf{S}(\boldsymbol{\rho}, \boldsymbol{\kappa}^{\text{inc}}) \cdot \mathbf{A}^{\text{inc}}(\boldsymbol{\kappa}^{\text{inc}}) \right] \right\rangle \\ &= \varepsilon \left\langle \int d^2 \boldsymbol{\kappa}^{\text{rinc}} \int d^2 \boldsymbol{\kappa}^{\text{inc}} \mathbf{A}^{\text{rinc}}(\boldsymbol{\kappa}^{\text{rinc}}) \cdot \mathbf{S}(\boldsymbol{\rho}, \boldsymbol{\kappa}^{\text{rinc}}) \cdot \boldsymbol{\sigma}_j \cdot \mathbf{S}(\boldsymbol{\rho}, \boldsymbol{\kappa}^{\text{inc}}) \cdot \mathbf{A}^{\text{inc}}(\boldsymbol{\kappa}^{\text{inc}}) \right\rangle \end{aligned} \quad (27)$$

After some algebra, using the orthogonality of the matrices in Eq. (24), and assuming the sample is stationary, Eq. (27) may be rewritten as

$$\mathbf{I}^{\text{tot}}(\boldsymbol{\rho}, z) = \int d^2 \boldsymbol{\kappa}^{\text{rinc}} \int d^2 \boldsymbol{\kappa}^{\text{inc}} \mathbf{M}[\mathbf{S}^\dagger(\boldsymbol{\rho}, \boldsymbol{\kappa}^{\text{rinc}}), \mathbf{S}(\boldsymbol{\rho}, \boldsymbol{\kappa}^{\text{inc}})] \cdot \langle \boldsymbol{\Sigma}[\mathbf{A}^{\text{rinc}}(\boldsymbol{\kappa}^{\text{rinc}}), \mathbf{A}^{\text{inc}}(\boldsymbol{\kappa}^{\text{inc}})] \rangle, \quad (28)$$

where the jk -th element of the matrix operator \mathbf{M} is

$$\mathbf{M}[\mathbf{S}^\dagger(\boldsymbol{\rho}, \boldsymbol{\kappa}^{\text{rinc}}), \mathbf{S}(\boldsymbol{\rho}, \boldsymbol{\kappa}^{\text{inc}})]_{jk} = \frac{1}{2} \text{Tr}[\mathbf{S}^\dagger(\boldsymbol{\rho}, \boldsymbol{\kappa}^{\text{rinc}}) \cdot \boldsymbol{\sigma}_j \cdot \mathbf{S}(\boldsymbol{\rho}, \boldsymbol{\kappa}^{\text{inc}}) \cdot \boldsymbol{\sigma}_k]. \quad (29)$$

The operation in Eq. (29) can be considered a cross-Mueller matrix. The matrix $\mathbf{M}[\mathbf{S}^\dagger, \mathbf{S}]$ is the Mueller matrix representation of the scattering matrix \mathbf{S} .⁴

We make a few assumptions that significantly simplify Eq. (28). We let the illumination region be much larger than the area on the sample that we are analyzing, so that the coherence in the illumination can be neglected. We also let the illumination and collection magnifications be large, so that the set of wavevectors leaving the source are parallel and the set incident upon the detector are parallel, so that we can neglect the differences between the polarization bases for the different propagation directions. Lastly, we will add polarization selectors near the source and near the detector (or any-

where in the optical path where the wavevectors are parallel) that pass a specific polarization state or allow us to measure the Stokes vector at the image plane. We thus make the approximation,

$$\langle \Sigma[\mathbf{A}^{\text{inc}\dagger}(\boldsymbol{\kappa}'^{\text{inc}}), \mathbf{A}^{\text{inc}}(\boldsymbol{\kappa}^{\text{inc}})] \rangle = \frac{k}{k_z} \mathbf{B} \delta(\boldsymbol{\kappa}^{\text{inc}} - \boldsymbol{\kappa}'^{\text{inc}}), \quad (30)$$

where \mathbf{B} is a constant Stokes vector associated with the illumination. Then Eq. (28) can be written as

$$\mathbf{I}^{\text{tot}}(\boldsymbol{\rho}, z) = \int d^2\boldsymbol{\kappa}^{\text{inc}} \frac{k}{k_z} \mathbf{M}[\mathbf{S}^\dagger(\boldsymbol{\rho}, \boldsymbol{\kappa}^{\text{inc}}), \mathbf{S}(\boldsymbol{\rho}, \boldsymbol{\kappa}^{\text{inc}})] \cdot \mathbf{B}. \quad (31)$$

From Eq. (31), it is apparent that we can consider the matrix

$$\int d^2\boldsymbol{\kappa}^{\text{inc}} \frac{k}{k_z} \mathbf{M}[\mathbf{S}^\dagger(\boldsymbol{\rho}, \boldsymbol{\kappa}^{\text{inc}}), \mathbf{S}(\boldsymbol{\rho}, \boldsymbol{\kappa}^{\text{inc}})] \quad (32)$$

to be the effective Mueller matrix describing the image of the sample in the microscope.

2.7. Aberrations

In a perfect optical system, plane waves arising from the object are transferred to plane waves incident on the image according to Eqs. (10) and (11). Aberrations, which express the deviations from the perfect system, are typically expressed in terms of the distortion of the nominal spherical waves arising from a point at the object and incident upon a point on the image plane.⁵ Because we are not expressing fields in terms of spherical waves or with rays, it not appropriate to use such nomenclature. Instead, we express aberrations in terms of how plane-waves arising from the object are distorted from ideal plane waves when they are incident upon the image plane. There is certainly a relationship between the two representations; however, that relationship will not be discussed here. We consider aberrations where the plane wave incident upon the sample has an additional phase Φ , which is a function of wavevector $\boldsymbol{\kappa}'$ and position $\boldsymbol{\rho}'$, and express that phase with the expansion

$$\Phi = \sum_{k,j,m,n} a_{klmn} (\boldsymbol{\kappa}')^n (\boldsymbol{\rho}')^k \begin{cases} \cos^l(\theta - \phi) & : l \geq 0 \\ \sin^l(\theta - \phi) & : l < 0 \end{cases} \begin{cases} \cos^m \theta & : m \geq 0 \\ \sin^m \theta & : m < 0 \end{cases}, \quad (33)$$

where a_{klmn} are coefficients for the aberrations,

$$\begin{aligned} \theta &= \arctan(\kappa'_y / \kappa'_x) \\ \phi &= \arctan(\rho'_y / \rho'_x) \end{aligned} \quad (34)$$

and k , l , m and n are integers with $|m| \leq n$, and $|l| \leq k$. For a rotationally-symmetric optical system, $m = 0$ and $l \geq 0$. The expression for the electric field at the image plane, which without aberrations is given by Eq. (9), then becomes

$$\mathbf{E}'(\boldsymbol{\rho}', z') = \int d^2\boldsymbol{\kappa}' \mathbf{A}'(\boldsymbol{\kappa}') e^{i(\boldsymbol{\kappa}' \cdot \boldsymbol{\rho}' + k'_z z' + \Phi)}. \quad (35)$$

Certain coefficients map onto specific common, known aberrations. For example, a_{1110} results in a change of magnification, a_{0020} changes the focus height, a_{2220} creates astigmatism, and a_{0040} corresponds to spherical aberration. Other aberrations can be thought of as combinations of these: distortion, a_{3110} , is a change of magnification proportional to ρ'^2 ; coma, a_{1130} , is a change of magnification proportional to κ'^2 ; and curvature of field, a_{2020} , is a change of focus proportional to ρ'^2 .

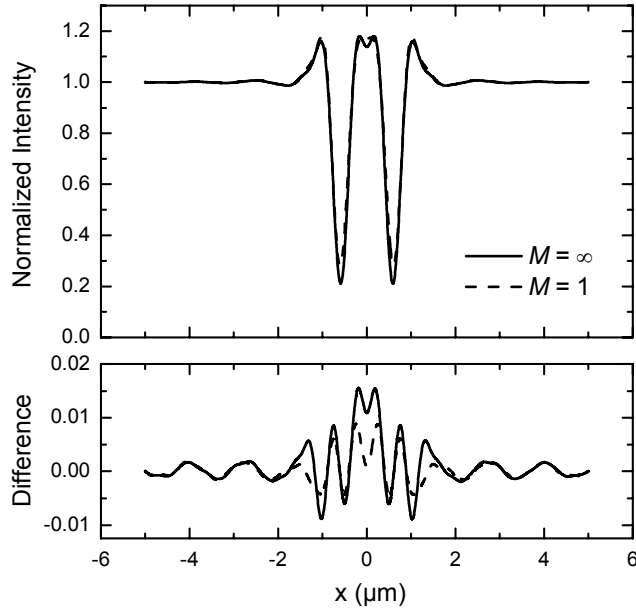


FIG. 1. Results of an inter-comparison between RCWA and IES calculations for a 1 μm wide, 0.4 μm high isolated silicon line on a silicon substrate. The top frame shows the normalized electric field intensity calculated by IES. The bottom frame shows the difference between the RCWA and IES calculations. The magnifications were (solid) ∞ and (dashed) 1.

3. RESULTS AND DISCUSSION

In this section, we present specific results of calculations of images using the methods described in Sec. 2. We first verify the equivalence of the RCWA and IES methods in Subsec. 3.1. Then, in Subsec. 3.2, we demonstrate by example how images depend upon the illumination area. Calculations of images as the focus height is varied are presented in Subsec. 3.3. In Subsec. 3.4, results of polarized imaging are presented. Finally, some effects of spherical aberration on the through-focus metric are described in Subsec. 3.5.

3.1. Comparison between sample models

An important consideration in any metrology where a theory is used to interpret the measurement results is the accuracy of that theory. While many theories are exact in their foundation, numerical problems associated with their implementation can limit their usefulness. It is difficult to obtain an uncertainty in a numerical calculation which has such unknowns as discrete approximations to integrals, truncations of series or expansions, or susceptibilities to round-off errors. Therefore, one would like to establish that the uncertainty in the simulation contributes an insignificant part to the total uncertainty. One way to do that is to use two very different approaches and compare their predictions.

Here, we compare results obtained from our implementations of the RCWA and IES methods. We chose a specific structure to study: an isolated 1 μm wide, 0.4 μm high line of silicon on a silicon substrate. The illumination wavelength was 0.546 μm , the illumination NA was 0.4, and the collection NA was 0.8. For the RCWA simulation, the period was 15 μm and 300 Fourier components were considered in the calculation. This particular structure was chosen, because the dimensions are large enough to display significant structure in the image.

Figure 1(bottom) shows the results of the comparison between the RCWA and IES methods for both $M = 1$ (electric field intensity only) and $M = \infty$. Since the curves lie very close to one another, the difference between them is also shown. That difference is never much larger than about 1.5 % of the signal at large distances. It is not known whether these differences result from errors in one, the other, or both of two methods. Another metric for comparison is the

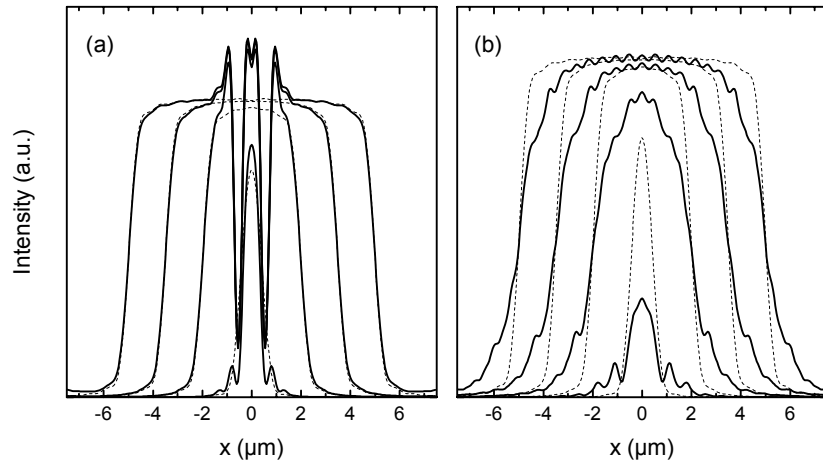


FIG. 2. Images of two structures (thick curves) as a function of illumination field stop, compared to those (thin dashed curves) from a perfectly reflecting substrate. The features were (a) a single $1\ \mu\text{m}$ wide, $0.4\ \mu\text{m}$ high silicon line on a silicon substrate, and (b) an infinite grating with $0.53975\ \mu\text{m}$ pitch of $0.229\ \mu\text{m}$ wide, $0.230\ \mu\text{m}$ high silicon lines on a silicon substrate. The wavelength was $0.546\ \mu\text{m}$, the illumination NA is 0.40 , and the collection NA is 0.80 . The source diaphragm diameters correspond, after magnification, to $1\ \mu\text{m}$, $4\ \mu\text{m}$, $7\ \mu\text{m}$, and $10\ \mu\text{m}$. The RCWA method is used for the sample calculations. The focus position was at the top of the features.

slope-square-weighted mean horizontal deviation between the curves, which for $|x| < 1\ \mu\text{m}$ is $1.6\ \text{nm}$ for $M = 1$ and $2.1\ \text{nm}$ for $M = \infty$. In the future, other structures will be investigated to gain further confidence in the accuracy of both methods.

Figure 1(top) shows the two cases of infinite and unit magnification. For the case of infinite magnification, the electric field intensity and magnetic field intensity are identical. However, for the case of unit magnification, the magnetic field intensity differs from the electric field intensity and is not shown. While the differences between the magnifications are not large, their differences are much larger than those observed between the RCWA and IES methods. Although it is not proven here, an image obtained with a magnification of 10 does not differ appreciably from one obtained with infinite magnification, so that for a typical microscope, the infinite magnification case is appropriate.

3.2. Effects of finite illumination

Figure 2 shows cross sections of images, taken perpendicular to the line direction and through the origin, of two structures for four different illumination diameters, compared to images of a perfectly reflecting substrate. The structures are a single $1\ \mu\text{m}$ wide, $0.4\ \mu\text{m}$ high silicon line on a silicon substrate in Fig. 2(a) and an infinite grating with $0.53975\ \mu\text{m}$ pitch of $0.229\ \mu\text{m}$ wide, $0.230\ \mu\text{m}$ high silicon lines on a silicon substrate in Fig. 2(b). In both cases, the wavelength of the light is $0.546\ \mu\text{m}$, the illumination NA is 0.40 , and the collection NA is 0.80 . The diameters of the field stops correspond, after magnification, to $1\ \mu\text{m}$, $4\ \mu\text{m}$, $7\ \mu\text{m}$, and $10\ \mu\text{m}$. The complex index of refraction at $0.546\ \mu\text{m}$ was assumed to be $4.091 + 0.026i$. The results are treated in the limit of infinite magnification. The images of the perfectly reflecting substrate are scaled to best match the data at the largest field stop diameter.

The larger the illumination area considered, the finer the grid that is needed in incident directions. Since the correlation function for every pair of incident directions must be considered [see, e.g., Eq. (17)], these calculations are very time consuming. Thus, it is impractical to perform these calculations routinely or for more realistic illumination areas (e.g., tens of micrometers). Instead, we would like to develop heuristic arguments by which we can feel comfortable that the infinite illumination condition can be assumed.

There are a few features observed in the results shown in Fig. 2 that should be pointed out. First, for the single line results [Fig. 2(a)], small differences can be observed between the perfect conductor image and the image far from the line; however, these differences are only observed near the edge of the illumination region. Secondly, for the single line, deviations of the line's image is only apparent for the $1\ \mu\text{m}$ and $4\ \mu\text{m}$ illumination diameters, with little deviation ob-

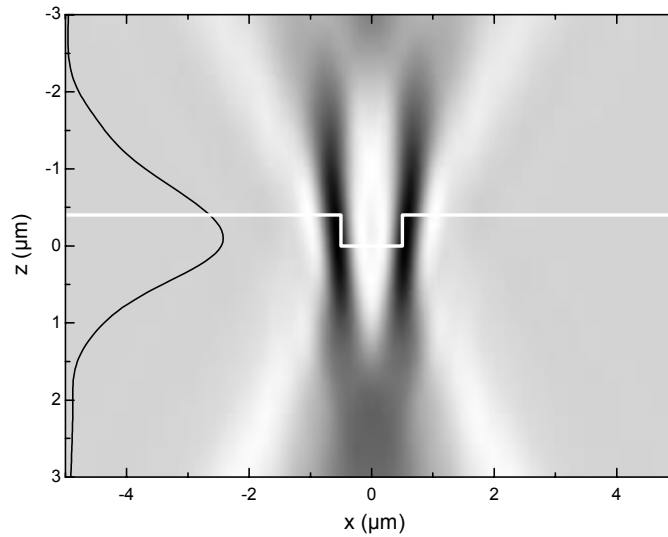


FIG. 3. Through-focus image of a 1 μm wide, 0.4 μm high silicon line on a silicon substrate. The outline of the feature is shown in white and the through-focus focus metric is shown as a black curve on the left side. The feature is a single 1 μm wide, 0.4 μm high silicon line on a silicon substrate, illuminated with wavelength 0.546 μm and NA is 0.40, and the collection NA is 0.80. The RCWA method is used for the sample calculations.

served between the 7 μm and 10 μm illumination diameters. Thirdly, for the infinite grating, there are significant deviations between the images of the grating and the images of the perfect conductor, with the edges of the images of the grating being much more smeared out. It is difficult to conclude that even for a 10 μm illumination diameter that the image has converged to a steady-state image at the center of the illuminated region. The combined results, however, suggest that one must remain at least as far as 5 μm from the edge of an illuminated region before interpreting results using an infinite illumination model.

3.3. Through-Focus Focus metric

Researchers at NIST have been investigating the behavior of images as a function of the focus position of the microscope.⁶ Modeling changes in focus is accomplished by the use of Eq. (5), where a shift in position of the sample is equivalent to a shift in the position by which the field is evaluated. The character of images measured through focus is quantified by a focus metric, defined by

$$F(z) = \int dx [dI(\rho, z)/dx]^2. \quad (36)$$

Analysis of the focus metric can be a sensitive method for characterizing critical dimensions. Figure 3 shows a representative image calculated as a function of focus height, with the through-focus focus metric.

3.4. Polarization effects

Figure 4 shows polarized images calculated for the 1 μm wide, 0.4 μm high silicon line on a silicon substrate, as a function of focus position. The two diagonal frames correspond to like-polarized images, while the off-diagonal frames correspond to cross-polarized images. The cross-polarized images are reduced significantly in intensity compared to the like-polarized images, but are not zero. All four images differ from one another. One might expect that measuring all four images would yield more information about the line or grating than that which would be obtained from a single image.

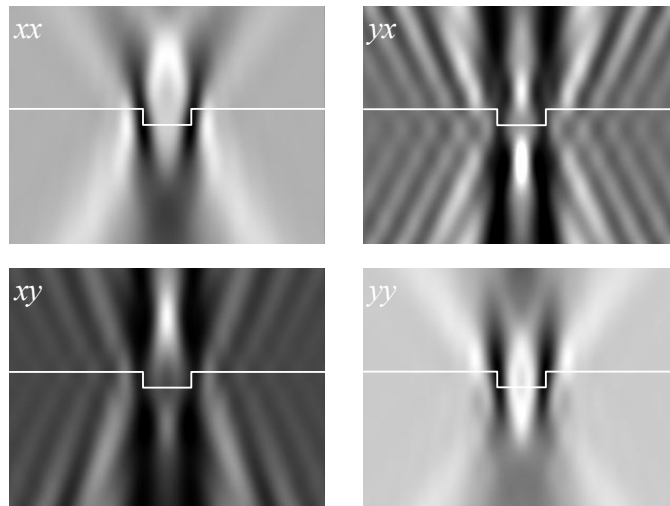


FIG. 4. Through focus polarization images of a single line, where the vertical direction, ranging over $6\ \mu\text{m}$, represents the focus position, and the horizontal direction, ranging over $7\ \mu\text{m}$, represents the x direction. The input-output polarizations are (upper left) xx , (upper right) yx , (lower left) xy , and (lower right) yy . The intensity scales of the xy and yx polarizations are expanded by a factor of 100 from those of the xx and yy polarizations. The feature is a single $1\ \mu\text{m}$ wide, $0.4\ \mu\text{m}$ high silicon line on a silicon substrate, illuminated with wavelength $0.546\ \mu\text{m}$ and NA is 0.40 , and the collection NA is 0.80 . The RCWA method is used for the sample calculations.

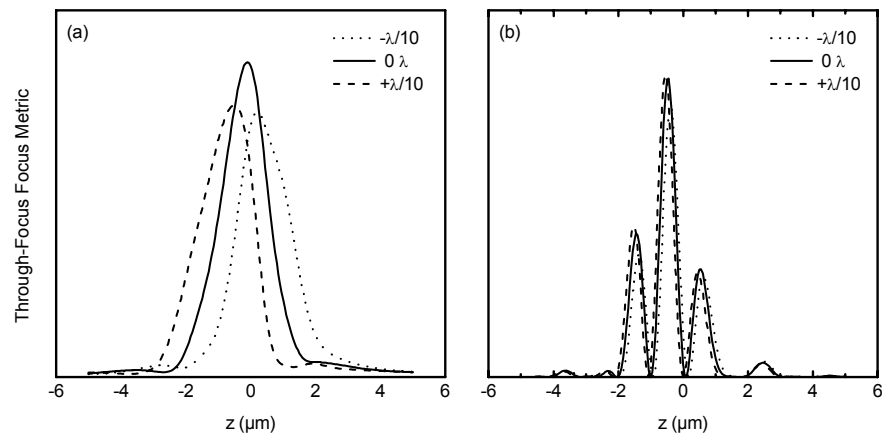


FIG. 5. Through-focus focus metric calculated with and without collection spherical aberration for two different structures, (a) a single $1\ \mu\text{m}$ wide, $0.4\ \mu\text{m}$ high silicon line on a silicon substrate, and (b) an infinite grating with $0.53975\ \mu\text{m}$ pitch of $0.229\ \mu\text{m}$ wide, $0.230\ \mu\text{m}$ high silicon lines on a silicon substrate. The magnitudes of the spherical aberration are (dashed) $+1/10$ wave, (solid) $0\ \lambda$, and (dotted) $-1/10$ wave. The wavelength is $0.546\ \mu\text{m}$, the illumination NA is 0.40 , and the collection NA is 0.80 . The RCWA method is used for the sample calculations. The focus position is measured with respect to the top of the features.

3.5. Aberrations

While a complete discussion of possible aberrations and their ramifications on quantitative imaging is a topic worthy of a treatise, we make a few observations here. Some aberrations, such as field curvature or tilt, shift the local z coordinate over the image, but do not affect the shape of local through-focus focus metric curves. Others, such as distortion, curve otherwise straight lines. Both effects can be quantitatively measured by moving or rotating the sample in the field

of view. However, the effects of others, such as spherical aberration, do not depend upon the field position, and extracting their magnitude from some simple measurements is not as simple.

We calculate through-focus focus metric curves for the two structures studied here, with and without spherical aberration. We chose an amount of aberration corresponding to one-tenth of a wave at the largest κ' for the collection NA of 0.8, which would be considered a relatively good specification for a high quality objective. The results, shown in Fig. 5, suggest that spherical aberration can have an adverse affect upon the shape of the curves. For the dense array of lines shown in Fig. 5(b), the aberration primarily shifts the curves and only changes their shape by a small amount. However, for the isolated line shown in Fig. 5(a), a much larger change in the curve is observed. A quantitative measurement of spherical aberration would clearly be required in order to extract information from real images.

4. FUTURE WORK

This work lays a foundation for predicting and modeling optical microscope images used in critical dimension and overlay metrology of semiconductor devices. Due to the lack of space, the number of examples that were given, and the extent to which information can be gleaned by these calculations, were limited. However, it is expected that a number of results will be presented in the near future:

- sensitivity of images and through-focus focus metric on critical dimensions of semiconductor lines;
- more complex illumination conditions, including those obtained from quantitative analysis of a real system;
- more complex polarization configurations, such as radial polarization or polarization-dependent illumination;
- further work on characterizing aberrations, including handling those on illumination; and
- comparisons between theory and experimental results.

ACKNOWLEDGEMENTS

The authors would like to acknowledge Richard Silver, Robert Larrabee, Ravikiran Attota, and Mark Davidson for various discussions leading to this work. One author (TAG) would also like to acknowledge the use of the NIST Raritan Cluster System in this work.

REFERENCES

1. R. Silver, R. Attota, M. Stocker, J. Jun, E. Marx, R. Larrabee, B. Russo, and M. Davidson, "Comparison of Measured Optical Image Profiles of Silicon Lines with Two Different Theoretical Models," in *Metrology, Inspection, and Process control for Microlithography XVI*, D.J. Herr, Ed., Proc. SPIE **4689**, 409–429 (2002).
2. M.G. Moharam, E.B. Grann, D.A. Pommet, and T.K. Gaylord, "Formulation for stable and efficient implementation of the rigorous coupled-wave analysis of binary gratings," J. Opt. Soc. Am. A **12**, 1068–1076 (1995).
3. M.G. Moharam, D.A. Pommet, E.B. Grann, and T.K. Gaylord, "Stable implementation of the rigorous coupled-wave analysis for surface-relief gratings: enhanced transmittance matrix approach," J. Opt. Soc. Am. A **12**, 1077–1086 (1995).
4. S. Huard, *Polarization of Light*, (John Wiley & Sons, Chichester, 1997), pp. 126–128.
5. M. Born and E. Wolf, *Principles of Optics*, (Pergamon, Oxford, 1980), Chapters 5 and 9.
6. R. Attota, R.M. Silver, T.A. Germer, M. Bishop, R. Larrabee, M.T. Stocker, and L. Howard, "Application of through-focus focus-metric analysis in high resolution optical metrology," in *Metrology, Inspection, and Process Control for Microlithography XIX*, R.M. Silver, Ed., Proc. SPIE **5752**, 1441–1449 (2005).